



1 **Combining of Mie-Raman and fluorescence observations: a step forward in aerosol**
2 **classification with lidar technology**

3

4 Igor Veselovskii¹, Qiaoyun Hu², Philippe Goloub², Thierry Podvin², Boris Barchunov¹, Mikhail
5 Korenskii¹

6 ¹*Prokhorov General Physics Institute of the Russian Academy of Sciences, Moscow, Russia.*

7 ²*Univ. Lille, CNRS, UMR 8518 - LOA - Laboratoire d'Optique Atmosphérique, F-59650 Lille,*
8 *France*

9 **Correspondence:** Qiaoyun Hu (qiaoyun.hu@univ-lille.fr)

10

11 **Abstract**

12 The paper presents an innovative approach to reveal variability of aerosol type at high spatio-
13 temporal resolution, by combining fluorescence and Mie-Raman lidar observations. The multi-
14 wavelength Mie-Raman lidar system in operation at the ATOLL platform (ATmospheric
15 Observatory of liLLe), Laboratoire d'Optique Atmosphérique, University of Lille, includes,
16 since 2019, a wideband fluorescence channel allowing the derivation of the fluorescence
17 backscattering coefficient β_F . The fluorescence capacity G_F , which is the ratio of β_F to the
18 aerosol backscattering coefficient, is an intensive particle's property, strongly changing with
19 aerosol type, thus providing a relevant basis for aerosol classification. In this first single version
20 of the algorithm, only two intensive properties are used for classification: the particle
21 depolarization ratio at 532 nm, and the fluorescence capacity, G_F . We applied our new
22 classification approach to ATOLL high performance lidar data obtained during 2020 – 2021
23 period, which includes strong smoke, dust and pollen episodes. It is demonstrated that separation
24 of the main particle's types and their mixtures can be performed with height resolution about 60
25 m and temporal resolution better than 10 minutes for the current lidar configuration.

26

27 **1. Introduction**

28 Atmospheric aerosol is one of the key factors influencing the Earth's radiation budget
29 through absorption and scattering of solar radiation and by affecting cloud formation. The
30 processes of aerosol–radiation and aerosol–cloud interaction depend on aerosol size, shape,
31 morphology, absorption, solubility, etc., thus knowledge of the chemical composition and mixing



32 state of the aerosol particles is important for modeling of aerosol impact (Boucher et al., 2013).
33 The aerosol properties may vary in a wide range, so in practice usually several main types of
34 aerosols are separated on a base of their origin: e.g. urban, dust, marine, biomass burning
35 (Dubovik et al., 2002). Successful remote characterization of column integrated aerosol
36 composition from the observations of Sun – sky photometers and spaceborne multiangle
37 polarimeters was demonstrated in numerous publications (Dubovik et al., 2002; Giles et al., 2012;
38 Hamill et al., 2016; Schuster et al., 2016; Li et al., 2019; Zhang et al., 2020). The aerosol impacts,
39 however, depends also on vertical variations/distributions of particle concentration and
40 composition, which cannot be derived from these instruments.

41 One of the recognized remote sensing techniques for vertical profiling of aerosol
42 properties is a lidar. Multiwavelength Mie-Raman and HSRL (High Spectral Resolution Lidar)
43 lidar systems provide unique opportunity to derive height-resolved particle intensive properties,
44 such as lidar ratios, Angstrom exponents and depolarization ratios at multiple wavelengths.
45 Based on this information, particle type can be determined (Burton et al., 2012, 2013; Groß et al.,
46 2013; Mamouri et al., 2017; Papagiannopoulos et al., 2018; Nicolae et al., 2018; Hara et al., 2018;
47 Voudouri et al., 2019; Wang et al., 2021; Mylonaki et al., 2021 and references therein). However,
48 there is a fundamental difference in particle classification based on the Sun – sky photometer and
49 on lidar observations. From both direct Sun and azimuth scanning measurements of the
50 photometer more than 100 observations are available. From this information the spectrally
51 dependent refractive index and absorption Angstrom exponent can be determined, which is
52 important for aerosol classification (Schuster et al., 2016; Li et al., 2019). The commonly used
53 multiwavelength lidars are based on a tripled Nd:YAG laser and are capable of providing three
54 backscattering (355 nm, 532 nm, 1064 nm), two extinction (355 nm, 532 nm) coefficients and up
55 to three particle depolarization ratios (so called $3\beta+2\alpha+3\delta$ set). Thus the number of available
56 lidar observations is eight or less which limits the performance of the aerosol typing algorithms.
57 Nevertheless, the results obtained by different research groups demonstrate that lidar-based
58 particle identification is possible. In publications of Burton et al. (2012, 2013) classification was
59 performed from four intensive parameters measured by the HSRL system: the lidar ratio at 532
60 nm (S_{532}), the backscattering Angstrom exponent for 532/1064 nm wavelengths ($BAE_{532/1064}$),
61 and particle depolarization ratios at 532 nm and 1064 nm (δ_{532} , and δ_{1064}). With these input



62 parameters eight aerosol types: smoke, fresh smoke, urban, polluted maritime, maritime, dusty
63 mix, pure dust and ice were discriminated.

64 Important information on aerosol vertical distribution comes from the
65 EARLINET/ACTRIS lidar-network, aiming at unifying multiwavelength Mie-Raman lidar
66 systems over Europe (Pappalardo et al., 2014). For the automation of aerosol classification,
67 several approaches were developed in the frame of EARLINET. These approaches include the
68 Mahalanobis distance-based typing algorithm (Papagiannopoulos et al., 2018), a neural network
69 aerosol classification algorithm (NATALI) (Nicolae et al., 2018), and algorithm based on source
70 classification analysis (SCAN) (Mylonaki et al., 2021). All these algorithms have demonstrated
71 their ability for aerosol classification. In particular, the NATALI is able to identify up to 14
72 aerosol mixtures from $3\beta+2\alpha+1\delta$ observations.

73 Nevertheless, the above-mentioned algorithms have to deal with a fundamental limitation:
74 the particle intensive properties, even for pure aerosols (generated by a single source) exhibit
75 strong variations. For example, the lidar ratio S_{355} of smoke in publication of Nicolae et al. (2018)
76 varies in 38 sr – 70 sr range, and in our own measurements we observed for aged smoke S_{355} as
77 low as 25 sr (Hu et al., 2021). Strong variation of smoke lidar ratios in EARLINET/ACTRIS
78 observations is discussed also in the recent publication of Adam et al. (2021). Such uncertainty
79 in parameters of the aerosol model complicates the aerosol classification. Thus, it is desirable to
80 combine the Mie-Raman observations with another range resolved technique, providing
81 additional independent information about aerosol composition. Such information can be obtained
82 from laser induced fluorescence emission.

83 Application of fluorescence lidar technique was intensively considered during the last
84 decade to study aerosol particles. Lidar measurements of the full fluorescence spectrum with
85 multianode photomultipliers (Sugimoto et al., 2012; Reichardt et al., 2014, 2017; Saito et al.,
86 2022) provides an obvious advantage in particle identification. However, even a more simple
87 fluorescence lidar with a single wideband fluorescence channel, opens new opportunities for
88 aerosol characterization (Veselovskii et al., 2021a; 2021b; Zhang et al., 2021). Such fluorescence
89 configuration could be implemented in existing Mie-Raman lidars, and the fluorescence
90 backscattering coefficient β_F is calculated from the ratio of fluorescence and nitrogen Raman
91 signals. To characterize the aerosol fluorescence properties, the fluorescence capacity G_F is
92 introduced as the ratio of β_F to aerosol backscattering coefficient at one of laser wavelengths



93 (Veselovskii et al., 2020). The fluorescence capacity is an intensive particle parameter, which
94 changes strongly with aerosol type, being the highest for smoke and the lowest for dust
95 (Veselovskii et al., 2021a). Thus, the combination of Mie – Raman and fluorescence backscatter
96 provides a basis to improve particle classification.

97 The goal of the present study is to develop a new approach for the evaluation of the
98 spatio-temporal variations of particle types in the troposphere, thus classification should be
99 performed with sufficient height and temporal resolutions. A Mie – Raman lidar provides several
100 particle intensive parameters, however, the profiles of particle parameters associated with the
101 extinction coefficient, such as lidar ratio or extinction Angstrom exponent, may contain strong
102 noises, because the extinction coefficients are derived from the slope of Raman lidar signals, thus
103 averaging over significant spatio-temporal intervals is demanded. Meanwhile, the particle
104 depolarization and the fluorescence *capacity* can be calculated with high spatio-temporal
105 resolution and in our recent publication (Veselovskii et al., 2021a) we have demonstrated that the
106 $\delta - G_F$ diagram allows to separate several aerosol types, such as dust, pollen, urban (continental)
107 and smoke.

108 In this paper, we present results of aerosol classification on a base of fluorescence and
109 Mie-Raman lidar measurements performed at the ATOLL (ATmospheric Observation at liLLe)
110 at Laboratoire d’Optique Atmosphérique, University of Lille, during 2020 – 2021 period, which
111 includes strong smoke, dust and pollen episodes. We start with a description of the experimental
112 setup and data processing scheme in Sect.2. In Sect.3 we present the algorithm for aerosol
113 classification on a base of depolarization and fluorescence measurements. Results of the
114 application of the developed approach to different atmospheric situations, including smoke, dust
115 and pollen episodes are given in Sect.4.

116

117 **2. Experimental setup and data analysis**

118 **2.1. Lidar system**

119 The multiwavelength Mie-Raman lidar LILAS (Lille Lidar AtmosphereS) is based on a
120 tripled Nd:YAG laser with a 20 Hz repetition rate and pulse energy of 70 mJ at 355 nm.
121 Backscattered light is collected by a 40 cm aperture Newtonian telescope and the lidar signals
122 are digitized with Licel transient recorders with 7.5 m range resolution, allowing simultaneous
123 detection in the analog and photon counting mode. The system is designed for the detection of



124 elastic and Raman backscattering, allowing the so called $3\beta+2\alpha+3\delta$ data configuration, including
125 three particle backscattering (β_{355} , β_{532} , β_{1064}), two extinction (α_{355} , α_{532}) coefficients along with
126 three particle depolarization ratios (δ_{355} , δ_{532} , δ_{1064}). The particle depolarization ratio, determined
127 as a ratio of cross- and co-polarized components of the particle backscattering coefficient, was
128 calculated and calibrated in the same way as described in Freudenthaler et al. (2009). Many
129 calibration and operation procedures have been automated for the LILAS system to improve the
130 overall performance of the lidar in terms of observation frequency and data quality. The aerosol
131 extinction and backscattering coefficients at 355 and 532 nm were calculated from Mie-Raman
132 observations (Ansmann et al., 1992), while β_{1064} was derived by the Klett method (Klett, 1985).
133 For calculation of α and β at 532 nm we use the rotational Raman scattering instead of the
134 vibrational one (Veselovskii et al., 2015), which allows to increase the power of Raman
135 backscatter and to decrease separation between the wavelengths of elastic and Raman
136 components. Additional information about atmospheric parameters was available from
137 radiosonde measurements performed at Herstmonceux (UK) and Beauvechain (Belgium) stations,
138 located 160 km and 80 km away from the observation site respectively.

139 The LILAS system can also profile the laser induced fluorescence of aerosol particles. A
140 part of the fluorescence spectrum is selected by a wideband interference filter of 44 nm width
141 centered at 466 nm (Veselovskii et al., 2020). The strong sunlight background at daytime
142 restricts the fluorescence observations to nighttime hours. The fluorescence backscattering
143 coefficient β_F is calculated from the ratio of fluorescence and nitrogen Raman backscattering
144 signal, as described in Veselovskii et al. (2020). This approach allows us to evaluate the absolute
145 values of β_F if the relative sensitivity of the channels is calibrated and the nitrogen Raman
146 scattering differential cross section is known. All β_F profiles presented in this work were
147 smoothed with the Savitzky – Golay method, using second order polynomials with 21 points in
148 the window. For the calculation of the fluorescence capacity G_F , in principle, backscattering
149 coefficients at any laser wavelength can be used. In our study we always used β_{532} , because it is
150 calculated with the use of rotational Raman component and is considered to be the most reliable,

151 thus the fluorescence capacity is calculated as $G_F = \frac{\beta_F}{\beta_{532}}$.

152 **2.2. Calculation of the particle backscattering coefficient from Mie-Raman measurements**



153 Mie – Raman lidar measurements allow independent evaluation of aerosol extinction and
 154 backscattering coefficients. Commonly used approach for β calculation was formulated in the
 155 paper of Ansmann et al. (1992). This approach includes the choice of a reference height, where
 156 the scattering is purely molecular. However, such range is not always available, for example, in
 157 the presence of the low level clouds. Moreover, when long-term spatio-temporal variations of
 158 backscattering coefficients are analyzed, the uncertainty in the choice of the reference height
 159 leads to oscillations in β profiles. To resolve this issue, we modified the Raman method as
 160 described below.

161 In an elastic channel, the backscattered radiative power P_L , at wavelength λ_0 and distance
 162 z is described by the lidar equation:

$$163 \quad P_L = O(z) \frac{1}{z^2} C_L (\beta_L^a + \beta_L^m) \exp \left\{ -2 \int_0^z (\alpha_L^a + \alpha_L^m) dz' \right\} = O(z) \frac{1}{z^2} C_L (\beta_L^a + \beta_L^m) T_L^2, \quad (1)$$

164 while in a Raman channel, it can be written as:

$$165 \quad P_R = O(z) \frac{1}{z^2} C_R \beta_R \exp \left\{ - \int_0^z (\alpha_L^a + \alpha_R^a + \alpha_L^m + \alpha_R^m) dz' \right\} = O(z) \frac{1}{z^2} C_R \beta_R T_L T_R. \quad (2)$$

166 Here $O(z)$ is the geometrical overlap factor, which is assumed to be the same for elastic and
 167 Raman channels. C_L and C_R are the range independent constants, including efficiency of the
 168 detection channel. T_L and T_R are one-way transmissions, describing light losses on the way from
 169 the lidar to distance z at laser λ_L and Raman λ_R wavelengths. Backscattering and extinction
 170 coefficients contain aerosol and molecular contributions: $\beta_L^a + \beta_L^m$ and $\alpha_L^a + \alpha_L^m$, where the
 171 superscripts “a” and “m” indicate aerosol and molecular scattering, respectively. Raman
 172 backscattering coefficient is:

$$173 \quad \beta_R = N \sigma_R, \quad (3)$$

174 where N is the number of Raman scatters (per unit of volume) and σ_R is the Raman differential
 175 scattering cross section in the backward direction.

176 Dividing equation (1) on (2) we get:

$$177 \quad \frac{P_L}{P_R} = \frac{C_L}{C_R} \frac{(\beta_L^a + \beta_L^m) T_L}{\beta_R T_R} \quad (4)$$

178 Backscattering coefficient is calculated from (3) and (4) as:



$$179 \quad \beta_L^a = \frac{P_L}{P_R} \frac{C_R}{C_L} \sigma_R N \frac{T_R}{T_L} - \beta_L^m = \frac{P_L}{P_R} KN \frac{T_R}{T_L} - \beta_L^m \quad (5)$$

180 The differential transmission $\frac{T_L}{T_R}$ can be calculated the same way, as it is done for the water
 181 vapor measurements (Whiteman, 2003). For rotational Raman signal, which we use in our 532
 182 nm channel (Veselovskii et al., 2015), $\lambda_L \approx \lambda_R$, so $\frac{T_L}{T_R} = 1$.

183 The calibration constant $K = \frac{C_R}{C_L} \sigma_R$ can be found by comparing β_L^a in Eq.5 with the
 184 backscattering coefficient $\tilde{\beta}_L^a$ computed with the traditional Raman method, using the reference
 185 height (Ansmann et al., 1992).

$$186 \quad K = (\tilde{\beta}_L^a + \beta_L^m) \frac{P_R}{P_L} \frac{1}{N} \frac{T_L}{T_R} \quad (6)$$

187 For simplicity, hereinafter we will use notation β_L instead β_L^a . Thus, if during the measurement
 188 session we have a temporal interval, where the reference height is available, we can determine
 189 the calibration constant K and use it for β_L calculations from eq.5, assuming that relative
 190 sensitivity of channels during the session is not changed. Even if cloud layers occur during the
 191 whole session, we can use K from the previous cloud-free profiles (assuming, again, that the
 192 relative sensitivity of channels is the same). We will call this approach for β calculation as
 193 “modified Raman method”, to distinguish it from traditional one (Ansmann et al., 1992).

194 To estimate variations of the relative sensitivity of the channels, we analyzed long-term
 195 cloudless measurements when the reference height was available for every individual profile.
 196 The results demonstrate that variations of calibration constant during the session (about 8 hours)
 197 were below 3%. Fig.1 and 2 present the application of this modified Raman method to the
 198 measurements on 2 March 2021. The dust layer extended from 2 km to 8 km height and inside
 199 this layer the ice and liquid clouds were formed during the 00:00 – 05:00 UTC interval, thus β_{532}
 200 could not be calculated with traditional Raman technique. The temporal interval 19:00 – 20:00
 201 was used to find calibration constant K . Fig.1 shows vertical profiles of backscattering
 202 coefficient $\tilde{\beta}_{532}$ calculated with traditional Raman method (with reference height), and β_{532}
 203 calculated with modified method (with the calibration constant). Profiles of $\tilde{\beta}_{532}$ and β_{532}



204 coincide for the whole height range. The calibration constant K , shown on the same plot, does
205 not demonstrate height dependence, though oscillations around the mean value increase with
206 height. For computations, we choose the value of K at low altitudes averaged inside some height
207 interval. Fig.2 provides spatio-temporal variations of β_{532} particle depolarization δ_{532} and the
208 fluorescence capacity G_F .

209 Depolarization measurements reveal the presence of dust ($\delta_{532}\approx 30\%$) and the ice cloud
210 above 4 km ($\delta_{532}>40\%$). The liquid cloud below 4 km after midnight can be identified by a low
211 depolarization ratio $\delta_{532}<3\%$. The fluorescence capacity of dust is low, about 0.2×10^{-4} . However,
212 below 2 km, G_F is significantly higher, up to 1.2×10^{-4} . In combination with a high depolarization
213 ratio (up to 20%), it can indicate the presence of pollen at low altitudes. On the fluorescence
214 capacity panel, we can clearly see that after 01:00 UTC the dust and pollen layers are mixed
215 below 2 km, resulting in a value of G_F about 0.5×10^{-4} . The fluorescence capacity inside ice and
216 liquid clouds is low, below 0.01×10^{-4} . Fig.2 clearly demonstrates the advantage of simultaneous
217 depolarization and fluorescence measurements for the study of cloud formation in the presence
218 of aerosol. All spatio-temporal distributions of β_{532} presented in this paper were calculated from
219 Eq.5 with a modified Raman method.

220

221 **3. Aerosol classification based on fluorescence measurements**

222 **3.1. Approach for aerosol classification.**

223 As was discussed in our recent publication (Veselovskii et al., 2021), the δ - G_F diagram
224 allows to separate several aerosol types, including smoke, dust, pollen, urban, ice and liquid
225 water particles. Smoke and urban aerosols both have a small depolarization ratio, but the
226 fluorescence capacity of smoke is almost one order higher, so these particles can be separated.
227 Dust and pollen both have high depolarization ratio (up to 30%), but G_F of dust is significantly
228 lower, which again provides basis for discrimination. The depolarization ratio of some aerosol
229 types is characterized by strong spectral dependence. For example, the depolarization ratio of
230 aged smoke decreases with wavelength. It is below 5% at 1064 nm but at 355 nm in upper
231 troposphere it may exceed 20% (Haarig et al., 2018; Hu et al., 2019; Veselovskii et al., 2021b),
232 which complicates smoke and dust separation. For pollen, on the contrary, the depolarization
233 ratio at 1064 nm can be the highest (Veselovskii et al., 2021a). Thus, choice of δ_{1064} for δ - G_F
234 diagram could be advantageous. However, as mentioned, the backscattering coefficient at 1064



235 nm is calculated with Klett method (Klett, 1985), which, besides assumption about lidar ratio,
236 needs reference height and cannot be used in cloudy situations. This is why in our study we used
237 the δ_{532} - G_F diagram.

238 In our present work, we consider a simple classification scheme since we use only two
239 intensive parameters G_F and δ_{532} . Our goal is to demonstrate that in the δ_{532} - G_F diagram, our lidar
240 observations form clusters and characteristic patterns which can be attributed to different aerosol
241 types or their mixtures. We consider four aerosol types: dust, smoke, pollen and urban, and two
242 cloud types: liquid and ice clouds. Dust and pollen are large particles of complicated shape,
243 while smoke and urban pollution are small particles with low depolarization. In our classification
244 “urban aerosol” includes continental aerosol, sulfates and soot. At this stage, we do not
245 discriminate particles by their absorption.

246 Typical ranges of G_F and δ_{532} variations for four aerosol types are given in Table 1 and
247 are shown in Fig.3. These ranges are based on results obtained in LOA and on particle
248 depolarization ratios commonly used for aerosol classification (Nicolae et al., 2018;
249 Papagiannopoulos et al., 2018, Mylonaki et al., 2021). The aerosol parameters, even for a single
250 type, may present significant variations. Moreover, actual aerosols exist usually as mixtures. For
251 example, the depolarization ratio δ_{532} of Saharan dust near the source regions is up to 35%
252 (Veselovskii et al., 2020a), but after transportation and mixing with local aerosol δ_{532} can be
253 below 20% (Rittmeister et al., 2017). In many studies, the dust with decreased depolarization
254 ratio is classified as “polluted dust” (e.g. Burton et al., 2012, 2013). At a moment, we do not
255 introduce the discrimination between the two subtypes and mark as “dust” the particles with
256 $15\% < \delta_{532} < 35\%$, and $0.1 \times 10^{-4} < G_F < 0.5 \times 10^{-4}$. Urban and smoke particles both have a low
257 depolarization ratio $\delta_{532} < 8\%$, but the fluorescence capacity of smoke is almost one order higher.

258 The pollen over north of France is usually mixed with other aerosols, and the particles,
259 which we mark as “pollen” are actually the mixtures containing pollen. Depolarization ratio of
260 clean pollen varies strongly for different taxa (Cao et al., 2010). For birch pollen, Cao et al.
261 (2010) reported $\delta_{532} = 33\%$, and in the measurements over Finland during birch pollination
262 (Bohlmann et al., 2019), observed values of δ_{532} up to 26%. In our classification scheme we type
263 as “pollen” the particles mixtures with $15\% < \delta_{532} < 30\%$, and $0.8 \times 10^{-4} < G_F < 3.0 \times 10^{-4}$. Thus, the
264 ranges of the parameters for different aerosol types chosen in Fig.3 and Table 1 include as
265 variation of “pure” aerosol parameters as their possible “contamination” by other particle types.



266

267 *Table 1. Ranges of particle depolarization δ_{532} and fluorescence capacity G_F , which were used*
 268 *for classification of four types of aerosols.*

Aerosol type	δ_{532} (%)	G_F ($\times 10^{-4}$)
Dust	15 - 35	0.1 – 0.5
Pollen	15 - 30	0.8 – 3.0
Urban	1 - 8	0.1 – 0.8
Smoke	1- 8	2.0 – 6.0

269

270 The mixing of aerosols should be revealed in δ_{532} - G_F diagram. For example, pollen can
 271 be mixed with urban particles. At different heights the pollen contributes differently to β_{532} , so at
 272 δ_{532} - G_F diagram, the data points will form the pattern, which extends from location, attributed to
 273 “pure” urban aerosol to location, attributed to “pure” pollen. To estimate, how such pattern looks
 274 like, a simplified modeling for fixed particle parameters was performed. Corresponding results
 275 are shown in Fig.3 by symbols (circles). The particle depolarization ratio δ of the mixture,
 276 containing urban aerosol (u) and pollen (p), with depolarization ratios δ^u and δ^p , can be
 277 calculated as:

$$278 \quad \delta = \frac{\left(\frac{\delta^p}{1+\delta^p}\right)\beta^p + \left(\frac{\delta^u}{1+\delta^u}\right)\beta^u}{\frac{\beta^p}{1+\delta^p} + \frac{\beta^u}{1+\delta^u}} \quad (7)$$

279 The fluorescence capacity of the mixture is given by:

$$280 \quad G_F = \frac{\beta^u G_F^u + \beta^p G_F^p}{\beta} \quad (8)$$

281 Here total backscattering $\beta = \beta^u + \beta^p$.

282 We assume that the depolarization ratios of pollen and urban aerosol are $\delta_{532}^p=30\%$ and $\delta_{532}^u=3\%$,
 283 while the fluorescence capacities are $G_F^u=0.2\times 10^{-4}$ and $G_F^p=2.5\times 10^{-4}$. The calculations in Fig.3
 284 were performed for values of pollen contribution $\frac{\beta_{532}^p}{\beta_{532}}$ in 0 - 1.0 range with step 0.1. In the δ_{532} -
 285 G_F diagram the computed points provide a characteristic curve, which in the next section will be
 286 compared with experimental results. The same computations were performed for a smoke (s) and
 287 dust (d) mixture, assuming $\delta_{532}^d=30\%$, $\delta_{532}^s=3\%$, $G_F^d=0.2\times 10^{-4}$ and $G_F^s=4.0\times 10^{-4}$. Corresponding



288 results are shown in Fig.3 with stars. In a similar way, the characteristic curves for other
289 mixtures can be also represented.

290 We are also able to identify liquid water and ice layers. Liquid water cloud layers have low
291 fluorescence capacity ($G_F < 0.01 \times 10^{-4}$) and $\delta_{532} < 3\%$. Ice particles also have low G_F , but at heights
292 where ice clouds are usually observed, the signal of fluorescence backscattering is noisy. Thus at
293 high altitudes ice particles are discriminated by a high depolarization ratio $\delta_{532} > 40\%$.

294

295 **3.2. Classification of spatio-temporal observations**

296 The input parameters in our classification scheme are the spatio-temporal distributions of
297 β_{532} , δ_{532} and G_F , which are presented as matrices $\beta_{532}^{i,j}$, $\delta_{532}^{i,j}$, $G_F^{i,j}$, where $i=1 \dots N_T$; $j=1 \dots N_H$.
298 Values N_T and N_H are the numbers of temporal and height intervals in the analyzed dataset. In a
299 single measurement we accumulate 2×10^3 laser pulses, so temporal resolution of the
300 measurements is about 100 s, while the height resolution is 7.5 m.

301 The particle intensive parameters cannot be evaluated reliably when the backscattering
302 coefficient is low. Thus, we set a threshold value for β_{532} (normally $0.2 \text{ Mm}^{-1} \text{ sr}^{-1}$); namely, when
303 $\beta_{532}^{i,j} < 0.2 \text{ Mm}^{-1} \text{ sr}^{-1}$ the elements of the matrices $\delta_{532}^{i,j}$ and $G_F^{i,j}$, are classified as “low signal” and
304 ignored. For the remaining elements, we determine the aerosol type, using our two-staged typing
305 algorithm. On the first stage, a primary typing is being made for each point (i,j) separately, in
306 accordance with parameter ranges given in the Table 1. The elements, which are out of all these
307 ranges, are marked as “undefined”. We consider 6 types of the particles, respectively dust, smoke,
308 pollen, urban, ice crystals and water droplets. Moreover, there can be two additional results of
309 primary typing: “undefined” and “low signal”. Thus, there are altogether 8 possible results of
310 primary typing.

311 The particle parameters, calculated with high spatio-temporal resolutions, contain
312 statistical noise which influences the results of the primary typing, thus producing high
313 frequency oscillations of non-physical character. From a physical point of view, the aerosol
314 single-type areas should form smooth regions, so a special smoothing procedure (stage 2 of our
315 algorithm) was developed to remove the oscillations. The smoothing procedure is based on a
316 convolution with Gaussian kernel



$$Z = \exp\left(-\left(\frac{t^2}{s_T^2} + \frac{h^2}{s_H^2}\right)\right) \quad (9)$$

317
318 where t and h are temporal and height coordinates. The resolution of typing is being controlled
319 by the parameters s_T and s_H , which are set as the number of temporal and height bins. In the
320 results presented we used $s_T=3$ and $s_H=5$, thus the temporal and height resolution of our typing
321 procedure is estimated to be about 8 minutes and 60 m respectively.

322

323 **4. Application of classification algorithm to LILAS data**

324 The classification algorithm, described in the previous section, was applied to the data of
325 the Mie-Raman- Fluorescence lidar at the ATOLL platform, located on the campus of Lille
326 University, during 2020 – 2021 period. Here we present results of aerosol classification for
327 several relevant atmospheric situations, to demonstrate that different aerosol types are well
328 separated based on δ_{532} - G_F diagram.

329 **12 September 2020: Wildfire smoke**

330 Fig.4 presents the spatio-temporal variations of aerosol and fluorescence backscattering
331 coefficients (β_{532} and β_F) together with the particle depolarization ratio δ_{532} and the fluorescence
332 capacity G_F during smoke episode on the night 12-13 September 2020. The smoke layer extends
333 from approximately 2 km to 5 km height, and it is characterized by high fluorescence capacity
334 $G_F > 3.0 \times 10^{-4}$ and low depolarization ratio $\delta_{532} < 7\%$. The cirrus clouds occurred above 11 km
335 height during the whole night. The smoke layer was transported from North America; detailed
336 analysis of the layer origin and transportation is given in the recent publication of Hu et al.
337 (2021). The results of aerosol typing for this episode are shown in Fig.5. On the δ_{532} - G_F diagram
338 these data form two clusters. First cluster includes points in the range $2.0 \times 10^{-4} < G_F < 6.0 \times 10^{-4}$ and
339 $2\% < \delta_{532} < 7\%$, such high fluorescence and low depolarization are typical for smoke particles. The
340 second cluster consists of points localized inside $0.1 \times 10^{-4} < G_F < 0.8 \times 10^{-4}$ and $1\% < \delta_{532} < 3\%$
341 intervals, which is typical of urban particles. After cluster localization, the observations can be
342 plotted as aerosol types, using the parameters in Table 1 and the FBC algorithm, described in
343 section 3.2. The aerosol types in Fig.5b are spatially separated and contain no high frequency
344 oscillations. Urban particles are localized at low heights, below 1 km. We would like to remind
345 that, at the condition of high relative humidity (RH), the fluorescence *capacity* can decrease due
346 to the particle's hygroscopic growth. In accordance with radiosonde data the relative humidity



347 below 1 km was quite high (about 70% at 500 m), which can explain the wide range of G_F
348 variation observed for urban particles in Fig.5a.

349

350 ***30 May 2020: Urban vs Pollen***

351 Pollen grains represent a significant fraction of primary biological materials in the
352 troposphere and fluorescence induced emission provides an opportunity for their identification.
353 Fig.6 presents spatio-temporal variations of β_{532} , β_F , δ_{532} , G_F during pollen season on the night
354 30-31 May 2020. Presence of different types of pollen over Lille in Spring – Summer 2020 was
355 discussed in our recent publication (Veselovskii et al., 2021). In accordance with radiosonde data
356 from Herstmonceux station, the RH at midnight was about 40% at 500 m and it increased up to
357 70% at 2000 m. The aerosol is located inside the planetary boundary layer (PBL) below 2.5 km.
358 At altitudes below 1 km, the depolarization ratio δ_{532} after 23:00 increases up to 20%
359 simultaneously with an increase of the fluorescence capacity above 2.0×10^{-4} , which can be an
360 indication of pollen presence.

361 On the δ_{532} - G_F diagram in Fig.7a, the data points spread from the values typical for the
362 urban particles to the values typical for the pollen. Contribution of pollen to the total
363 backscattering changes with height and the points form the pattern, similar to characteristic curve,
364 calculated for urban – pollen mixture in Fig.3. The spatio-temporal distribution of aerosol types
365 is shown in Fig.7b. The urban particles are predominant, while pollen is localized below 1 km
366 height. The grey color corresponds to unidentified aerosol type, which in our case is the mixture
367 of urban particles and pollen.

368 One indicator of pollen presence in an aerosol mixture, can be a higher value of δ_{1064} in
369 respect to δ_{532} (Veselovskii et al., 2021). Fig.8a shows the vertical profile of the backscattering
370 coefficient β_{532} averaged over 23:00 – 01:00 UTC period together with the particle
371 depolarization ratios δ_{532} and δ_{1064} . The ratio $\frac{\delta_{1064}}{\delta_{532}}$ is about 1.5 at 0.75 km height, which
372 corroborates suggestions about pollen presence. Both depolarization ratios decrease with height,
373 simultaneously with decrease of fluorescence capacity, as follows from Fig.8b. The
374 backscattering Angstrom exponent (BAE) $A_{532/1064}^\beta$ in Fig.8b is about 1.25 and it does not
375 demonstrate significant variations in 0.7 km – 2.25 km height range. The reason can be that the



376 contribution of pollen to the total backscattering is not high and the corresponding effect can be
377 masked by other processes, such as particle hygroscopic growth.

378

379 ***14 September 2020: wildfire smoke vs pollen mixture***

380 Another strong smoke episode occurred in the night 14-15 September 2020, and
381 corresponding distributions of β_{532} , β_F , δ_{532} , and G_F are shown Fig.9. The elevated smoke layer
382 with low depolarization ratio ($\delta_{532} < 5\%$) and high fluorescence capacity (up to 4.0×10^{-4}) was
383 observed at approximately 6 km height during the whole night. Inside the PBL the depolarization
384 ratio is higher, up to 15%, while fluorescence capacity is low, compared to the elevated layer
385 (about 1.0×10^{-4}). On the δ_{532} - G_F diagram in Fig.10a we can see the cluster of data points,
386 corresponding to the smoke. The same time, a part of the points are inside the range of
387 parameters attributed to the pollen (Table 1). The remaining points should be attributed to the
388 mixture of pollen, smoke and urban aerosol. On the distribution of the particle types (Fig.10b)
389 this mixture is marked with gray color. The pollen particles are localized below 1 km. Presence
390 of pollen over Lille in September is not common, but it can be transported from other regions.
391 The transport of pollen can be analyzed with a global-to-meso-scale dispersion model SILAM
392 (Sofiev et al., 2006). The SILAM pollen index for this date demonstrates the transport of pollen
393 to northern France from the southeast of France and the east Mediterranean.

394 Fig.11a presents profiles of δ_{532} and δ_{1064} together with β_{532} for the temporal interval
395 00:00 – 04:00 UTC. The relative humidity, in accordance with radiosonde data from
396 Herstmonceux station, did not exceed 50% below 1.7 km. Above that height RH increased up to
397 75% at 2.5 km, thus the observed increase of β_{532} above 1.5 km can be partly related to RH
398 growth. The relative humidity inside the smoke layer did not exceed 10%. Similarly to Fig.8,

399 δ_{1064} exceeds δ_{532} at low heights. The ratio $\frac{\delta_{1064}}{\delta_{532}}$ is about 1.5 at 1 km and inside the smoke layer

400 $\frac{\delta_{1064}}{\delta_{532}} \approx 0.4$. Higher values of depolarization ratio at 532 nm compared to 1064 nm are typical for

401 aged smoke (Haarig et al., 2018; Hu et al., 2019, 2021). The BAE does not present significant

402 height variations: $A_{532/1064}^\beta$ is about 1.0 inside the PBL and it increases to 1.25 inside the smoke

403 layer (Fig.11b). Simultaneously, the fluorescence capacity in the smoke layer increases about a



404 factor 4, comparing to the PBL, which demonstrates efficiency of the fluorescence technique for
405 discriminating smoke from other aerosol types.

406

407 ***10 April 2020: Urban vs Pollen***

408 In the beginning of April, we experienced several atmospheric situations, for which
409 elevated layers were classified as urban aerosols. One of such cases, on the night 10 -11 April
410 2020, is shown in Fig.12. Lidar observations were performed at an angle of 45 degrees to the
411 horizontal, so the minimum height reachable in the analysis is 350 m. The relative humidity, in
412 accordance with radiosonde data from Herstmonceux station, increased with height from 54% at
413 1.0 km to 65% at 2.2 km. The layer with depolarization ratio δ_{532} below 5% was observed at
414 about 2 km height during the night. The fluorescence capacity in the layer is low (below 0.5×10^{-4}
415 ⁴), so it is identified as urban aerosol. For the period 21:00 – 23:00 UTC the depolarization ratio
416 below 500 m has increased simultaneously with the fluorescence capacity, which can be an
417 indication of pollen presence.

418 On the δ_{532} - G_F diagram (Fig.13a) most of the points are classified as urban aerosol.
419 However, at low altitudes the particles have relatively high depolarization ratios $\delta_{532} > 15\%$, and
420 the points on δ_{532} - G_F diagram provide the pattern typical for urban – pollen mixture. Our
421 algorithm identifies particles mainly as urban aerosol (Fig.12b), and the regions with grey color
422 at low heights, correspond to urban – pollen mixture.

423 The presence of pollen is supported by the profiles of δ_{532} and δ_{1064} shown in Fig.14. At
424 low heights δ_{1064} exceeds δ_{532} and the ratio $\frac{\delta_{1064}}{\delta_{532}}$ is about 1.4 at 0.5 km. However, inside the
425 elevated layer this ratio decreases and becomes about 0.8 at 2.25 km, which indicates that
426 mixture composition changed and the pollen contribution decreased. In the same height range the
427 fluorescence capacity decreases from 0.38×10^{-4} to 0.28×10^{-4} , while BAE gradually increases
428 from 0.75 to 1.25, which can be due to decrease of pollen contribution.

429

430 ***11 August 2021: contacting layers of smoke and urban aerosol***

431 Separation of smoke and urban particles is a challenging task for Mie – Raman lidar,
432 because both types have small effective radius, and similar depolarization ratios δ_{532} . However,
433 the fluorescence capacity of smoke is about factor 4-5 higher than that of urban aerosol, which



434 allows their reliable separation. The analyses of the measurements in the night 11-12 August
435 2021 are shown in Fig.15. The RH decreases with height from 70% to 40% inside 500 m – 2250
436 m range. The main part of aerosol is concentrated below 2500 m and two height intervals can be
437 distinguished. Above approximately 1500 m the layer with high fluorescence capacity (up to
438 3.0×10^{-4}) is observed, while in the layer below 1500 m, the G_F is low, (below 0.8×10^{-4}).

439 On the δ_{532} - G_F diagram in Fig.16a one cluster of points is localized mainly inside the
440 interval $2.0 \times 10^{-4} < G_F < 4.0 \times 10^{-4}$ and $4\% < \delta_{532} < 10\%$. Such properties can be attributed to smoke.
441 The points in Fig.16a form also a pattern typical for urban – pollen mixture. From the
442 distribution of aerosol types in Fig.16b we conclude that the points in the first cluster correspond
443 to the upper smoke layer, while the lower layer is represented by urban particles and by their
444 mixture with pollen. The pollen becomes predominant below 800 m during 20:00 – 22:00 UTC.
445 The smoke and urban layers are in contact and the particle mixing occurs, which increases
446 dispersion within the clusters.

447

448 **1 April 2021: Dust**

449 Dust layers transported from Africa are regularly observed over North Europe and
450 especially North of France. One such dust episode took place in the night 1-2 April 2020 and the
451 corresponding spatio-temporal variations of β_{532} , β_F , δ_{532} , and G_F are shown in Fig.17. The dust
452 layer, with depolarization ratio exceeding 30%, and low fluorescence, extends from
453 approximately 1.0 km to 5.0 km height. The fluorescence capacity varied inside the layer. In the
454 center it was the lowest (about 0.1×10^{-4}), but at the bottom of the layer and near the top, G_F
455 increased up to $(0.2 \div 0.3) \times 10^{-4}$, probably due to the mixing with local pollution. In Fig.18a, (δ_{532} -
456 G_F diagram), we observed a typical cluster of dust particles. There is also a second small cluster
457 which is attributed to urban aerosols. On the distribution of particle types in Fig.18b the urban
458 aerosol occurs below 800 m after 23:00 UTC.

459

460 **Conclusion**

461 The results presented in this study can be considered as the first important step in the
462 combination of Mie – Raman and fluorescence lidar data. In this version of our algorithm, only
463 two intensive parameters are used for classification: the particle depolarization ratio δ_{532} and the
464 fluorescence capacity G_F . These parameters are chosen because they are specific for different



465 types of aerosol and can be calculated with high spatio-temporal resolution. Moreover, δ_{532} and
466 G_F can be calculated at lower altitudes, compared to extinction related parameters, such as lidar
467 ratio and extinction Angstrom exponent. Thus classification, in principle, is possible at ranges
468 with incomplete geometrical overlap. Finally, computation of β_F does not demand the use of
469 reference height, only calibration of relative sensitivity of the channels is needed. In our version
470 of algorithm for β_{532} calculation, we also use calibration constant instead of the reference height.
471 Thus, aerosol classification is possible, even in the presence of low level clouds.

472 Though only two input parameters are considered in the classification algorithm, the use
473 of fluorescence measurements provides advances in aerosol classification. Analysis of numerous
474 observations, performed at Lille University for the period 2020 – 2021 demonstrates the
475 possibility to separate four types of aerosols, such as dust, smoke, pollen and urban. Moreover,
476 we are able to identify the layers containing the liquid water particles and ice. The number of
477 determined aerosol classes can be increased, by considering the particle mixtures. In particular,
478 “pure” dust can be considered separately from “polluted” one. Polluted dust can be discriminated
479 by lower values of the depolarization ratio and by higher the fluorescence capacity.

480 Fluorescence technique is especially promising for separation of smoke and urban
481 particles, because fluorescence capacity of smoke is about factor five higher. The important
482 advantage of fluorescence measurements is the ability to identify the biological particles in the
483 atmosphere, such as pollen, which are usually not included in the classification schemes, based
484 on Mie-Raman observations. At the same time, our observations demonstrate that biological
485 particles are frequently observed during Spring – Autumn seasons and may contribute
486 significantly to the aerosol composition inside the PBL. The developed approach allows to
487 identify aerosol types with high spatio-temporal resolutions, which is estimated to be 60 m for
488 height and less than 10 minutes for time, for the current instrumental configuration. Such
489 resolution provides an opportunity for investigating the dynamics of aerosol mixing in the
490 troposphere.

491 The next step in algorithm development will be the increase of input parameters number.
492 We plan to include the backscattering Angstrom exponents and the depolarization spectral ratios
493 ($\delta_{355}/\delta_{532}$ and $\delta_{532}/\delta_{1064}$), which can be also calculated with high spatio-temporal resolutions. The
494 fluorescence capacity depends on the relative humidity, due to the effects of hygroscopic growth.
495 Thus, information about spatio-temporal distribution of RH should be included in the analysis. It



496 is also important to combine our algorithm with existing classification schemes, which we plan
497 to consider in the near future.

498

499 **Data availability.** Lidar measurements are available upon request
500 (philippe.goloub@univ-lille.fr).

501

502 **Author contributions.** IV processed the data and wrote the paper. QH and TP performed the
503 measurements. PG supervised the project and helped with paper preparation. BB prepared
504 algorithm for aerosol classification. MK developed software for data processing.

505

506 **Competing interests.** The authors declare that they have no conflict of interests.

507

508 **Acknowledgement**

509 We acknowledge funding from the CaPPA project funded by the ANR through the PIA under
510 contract [ANR-11-LABX-0005-01](#), the “Hauts de France” Regional Council (project CLIMIBIO)
511 and the European Regional Development Fund (FEDER). ESA/QA4EO program is greatly
512 acknowledged for support of observation activity at LOA.

513

514 **References**

- 515 Adam, M., Stachlewska, I. S., Mona, L., Papagiannopoulos, N., Bravo-Aranda, J. A., Sicard, M.,
516 Nicolae, D. N., Belegante, L., Janicka, L., Szczepanik, D., Mylonaki, M., Papanikolaou, C.-A.,
517 Siomos, N., Voudouri, K. A., Alados-Arboledas, L., Apituley, A., Mattis, I., Chaikovskiy, A.,
518 Muñoz-Porcar, C., Pietruczuk, A., Bortoli, D., Baars, H., Grigorov, I., and Peshev, Z.:
519 Biomass burning events measured by lidars in EARLINET – Part 2: Optical properties
520 investigation, *Atmos. Chem. Phys. Discuss.*, <https://doi.org/10.5194/acp-2021-759>, in review,
521 2021.
- 522 Ansmann, A., Riebesell, M., Wandinger, U., Weitkamp, C., Voss, E., Lahmann, W., and
523 Michaelis, W.: Combined Raman elastic-backscatter lidar for vertical profiling of moisture,
524 aerosols extinction, backscatter, and lidar ratio, *Appl.Phys.B*, *55*, 18-28, 1992.
- 525 Bohlmann, S., Shang, X., Giannakaki, E., Filioglou, M., Saarto, A., Romakkaniemi, S. and
526 Komppula, M.: Detection and characterization of birch pollen in the atmosphere using multi-
527 wavelength Raman lidar in Finland, *Atmos. Chem. Phys.* *19*, 14559–14569, 2019.
528 doi.org/10.5194/acp-19-14559-2019.



- 529 Boucher, O., Randall, D., Artaxo, P., Bretherton, C., Feingold, G., Forster, P., Kerminen, V.-M.,
530 Kondo, Y., Liao, H., Lohmann, U., Rasch, P., Satheesh, S. K., Sherwood, S., Stevens, B., and
531 Zhang, X. Y.: Clouds and Aerosols, in: *Climate Change 2013: The Physical Science Basis*.
532 Contribution of Working Group I to the Fifth Assessment Report of the Intergovernmental
533 Panel on Climate Change, edited by: Stocker, T. F., Qin, D., Plattner, G.-K., Tignor, M., Allen,
534 S. K., Boschung, J., Nauels, A., Xia, Y., Bex, V., and Midgley, P., M., Cambridge University
535 Press, Cambridge, United Kingdom and New York, NY, USA, 2013
- 536 Burton, S. P., Ferrare, R. A., Hostetler, C. A., Hair, J. W., Rogers, R. R., Obland, M. D., Butler, C.
537 F., Cook, A. L., Harper, D. B., and Froyd, K. D.: Aerosol classification using airborne High
538 Spectral Resolution Lidar measurements – methodology and examples, *Atmos. Meas. Tech.*, 5,
539 73–98, 2012. <https://doi.org/10.5194/amt-5-73-2012>
- 540 Burton, S. P., Ferrare, R. A., Vaughan, M. A., Omar, A. H., Rogers, R. R., Hostetler, C. A., and
541 Hair, J. W.: Aerosol classification from airborne HSRL and comparisons with the CALIPSO
542 vertical feature mask, *Atmos. Meas. Tech.*, 6, 1397–1412, 2013. [https://doi.org/10.5194/amt-](https://doi.org/10.5194/amt-6-1397-2013)
543 [6-1397-2013](https://doi.org/10.5194/amt-6-1397-2013)
- 544 Cao, X., Roy, G., and Bernier, R.: Lidar polarization discrimination of bioaerosols, *Opt. Eng.*, 49,
545 116201, <https://doi.org/10.1117/1.3505877>, 2010.
- 546 Dubovik, O., Holben, B. N., Eck, T. F., Smirnov, A., Kaufman, Y. J., King, M. D., Tanre, D.,
547 and Slutsker, I.: Variability of absorption and optical properties of key aerosol types observed
548 in worldwide locations, *J. Atmos. Sci.*, 59, 590–608, 2002.
- 549 Freudenthaler, V., Esselborn, M., Wiegner, M., Heese, B., Tesche, M. and co-authors:
550 Depolarization ratio profiling at several wavelengths in pure Saharan dust during SAMUM
551 2006, *Tellus* 61B, 165–179, 2009.
- 552 Giles, D. M., Holben, B. N., Eck, T. F., Sinyuk, A., Smirnov, A., Slutsker, I., Dickerson, R. R.,
553 Thompson, A. M., and Schafer, J. S.: An analysis of AERONET aerosol absorption properties
554 and classifications representative of aerosol source regions, *J. Geophys. Res.* 117, D17203,
555 <https://doi.org/10.1029/2012JD018127>, 2012.
- 556 Groß, S., Esselborn, M., Weinzierl, B., Wirth, M., Fix, A., and Petzold, A.: Aerosol classification
557 by airborne high spectral resolution lidar observations, *Atmos. Chem. Phys.*, 13, 2487–2505,
558 2013. <https://doi.org/10.5194/acp-13-2487-2013>



- 559 Haarig, M., Ansmann, A., Baars, H., Jimenez, C., Veselovskii, I., Engelmann, R., and Althausen,
560 D.: Depolarization and lidar ratios at 355, 532, and 1064 nm and microphysical properties of
561 aged tropospheric and stratospheric Canadian wildfire smoke, *Atmospheric Chemistry and*
562 *Physics*, 18, 11 847–11 861, 2018.
- 563 Hamill, P., Giordano, M., Ward, C., Giles, D., and Holben, B.: An AERONET-based aerosol
564 classification using the Mahalanobis distance, *Atmos. Environ.*, 140, 213–233,
565 <https://doi.org/10.1016/j.atmosenv.2016.06.002>, 2016.
- 566 Hara, Y., Nishizawa, T., Sugimoto, N., Osada, K., Yumimoto, K., Uno, I., Kudo, R., and
567 Ishimoto, H.: Retrieval of aerosol components using multi-wavelength Mie-Raman lidar and
568 comparison with ground aerosol sampling, *Remote Sens.*, 10, 937, 2018.
569 <https://doi:10.3390/rs10060937>
- 570 Hu, Q., Goloub, P., Veselovskii, I., Bravo-Aranda, J.-A., Popovici, I. E., Podvin, T., Haeffelin,
571 M., Lopatin, A., Dubovik, O., Pietras, C., et al.: Long-range-transported Canadian smoke
572 plumes in the lower stratosphere over northern France, *Atmospheric Chemistry and Physics*,
573 19, 1173–1193, 2019.
- 574 Hu, Q., Goloub, P., Veselovskii, I., and Podvin, T.: The characterization of long-range
575 transported North American biomass burning plumes: what can a multi-wavelength Mie-
576 Raman-polarization-fluorescence lidar provide?, *Atmos. Chem. Phys. Discuss.* [preprint],
577 <https://doi.org/10.5194/acp-2021-971>, in review, 2021.
- 578 Klett J.D., “Lidar inversion with variable backscatter/extinction ratios”, *Appl.Opt.* 24, 1638-1643,
579 1985.
- 580 Li, L., Dubovik, O., Derimian, Y., Schuster, G. L., Lapyonok, T., Litvinov, P., Ducos, F., Fuertes,
581 D., Chen, C., Li, Z., Lopatin, A., Torres, B., and Che, H.: Retrieval of aerosol components
582 directly from satellite and ground-based measurements, *Atmos. Chem. Phys.*, 19, 13409–
583 13443, 2019. <https://doi.org/10.5194/acp-19-13409-2019>
- 584 Mamouri, R.-E., and Ansmann, A.: Potential of polarization/Raman lidar to separate fine dust,
585 coarse dust, maritime, and anthropogenic aerosol profiles, *Atmos. Meas. Tech.*, 10, 3403–
586 3427, 2017. <https://doi.org/10.5194/amt-10-3403-2017>
- 587 Mylonaki, M., Giannakaki, E., Papayannis, A., Papanikolaou, C.-A., Komppula, M., Nicolae, D.,
588 Papagiannopoulos, N., Amodeo, A., Baars, H., and Soupiona, O.: Aerosol type classification



- 589 analysis using EARLINET multiwavelength and depolarization lidar observations, *Atmos.*
590 *Chem. Phys.*, 21, 2211–2227, 2021. <https://doi.org/10.5194/acp-21-2211-2021>
- 591 Nicolae, D., Vasilescu, J., Talianu, C., Biniotoglou, I., Nicolae, V., Andrei, S., and Antonescu, B.:
592 A neural network aerosol-typing algorithm based on lidar data, *Atmos. Chem. Phys.*, 18,
593 14511–14537, 2018. <https://doi.org/10.5194/acp-18-14511-2018>
- 594 Papagiannopoulos, N., Mona, L., Amodeo, A., D’Amico, G., Gumà Claramunt, P., Pappalardo,
595 G., Alados-Arboledas, L., Guerrero-Rascado, J. L., Amiridis, V., Kokkalis, P., Apituley, A.,
596 Baars, H., Schwarz, A., Wandinger, U., Biniotoglou, I., Nicolae, D., Bortoli, D., Comerón, A.,
597 Rodríguez-Gómez, A., Sicard, M., Papayannis, A., and Wiegner, M.: An automatic
598 observation-based aerosol typing method for EARLINET, *Atmos. Chem. Phys.*, 18, 15879–
599 15901, 2018. <https://doi.org/10.5194/acp-18-15879-2018>
- 600 Pappalardo, G., Amodeo, A., Apituley, A., Comeron, A., Freudenthaler, V., Linné, H., Ansmann,
601 A., Bösenberg, J., D’Amico, G., Mattis, I., Mona, L., Wandinger, U., Amiridis, V., Alados-
602 Arboledas, L., Nicolae, D., and Wiegner, M.: EARLINET: towards an advanced sustainable
603 European aerosol lidar network, *Atmos. Meas. Tech.*, 7, 2389–2409, 2014.
604 <https://doi.org/10.5194/amt-7-2389-2014>, 2014.
- 605 Reichardt, J., Leinweber, R., Schwebe, A.: Fluorescing aerosols and clouds: investigations of
606 co-existence, *Proceedings of the 28th ILRC, Bucharest, Romania, 25-30 June, 2017.*
- 607 Rittmeister, F., Ansmann, A., Engelmann, R., Skupin, A., Baars, H., Kanitz, T., and Kinne, S.:
608 Profiling of Saharan dust from the Caribbean to western Africa –Part 1: Layering structures
609 and optical properties from shipborne polarization/Raman lidar observations, *Atmos. Chem.*
610 *Phys.*, 17, 12963–12983, 2017. <https://doi.org/10.5194/acp-17-12963-2017>
- 611 Saito, Y., Hosokawa, T., Shiraishi, K.: Collection of excitation-emission-matrix fluorescence of
612 aerosol-candidate-substances and its application to fluorescence lidar monitoring, *Appl. Opt.*,
613 61, 653 – 660, 2022.
- 614 Schuster, G. L., Dubovik, O., and Arola, A.: Remote sensing of soot carbon – Part 1:
615 Distinguishing different absorbing aerosol species, *Atmos. Chem. Phys.*, 16, 1565–1585,
616 <https://doi.org/10.5194/acp-16-1565-2016>, 2016.
- 617 Sofiev, M., Siljamo, P., Valkama, I., Ilvonen, M., & Kukkonen, J.: A dispersion modelling
618 system SILAM and its evaluation against ETEX data, *Atmospheric Environment*, 40, 674-
619 685, 2006. <https://doi.org/10.1016/j.atmosenv.2005.09.069>



- 620 Sugimoto, N., Huang, Z., Nishizawa, T., Matsui, I., Tatarov, B.: Fluorescence from atmospheric
621 aerosols observed with a multichannel lidar spectrometer," *Opt. Expr.* 20, 20800–20807, 2012.
- 622 Veselovskii, I., Whiteman, D. N., Korenskiy, M., Suvorina, A., Perez-Ramirez, D.: Use of
623 rotational Raman measurements in multiwavelength aerosol lidar for evaluation of particle
624 backscattering and extinction, *Atmos. Meas. Tech.*, 8, 4111–4122, 2015.
- 625 Veselovskii, I., Hu, Q., Goloub, P., Podvin, T., Korenskiy, M., Derimian, Y., Legrand, M., and
626 Castellanos, P.: Variability in lidar-derived particle properties over West Africa due to
627 changes in absorption: towards an understanding, *Atmos. Chem. Phys.*, 20, 6563–6581, 2020a.
628 <https://doi.org/10.5194/acp-20-6563-2020>
- 629 Veselovskii, I., Hu, Q., Goloub, P., Podvin, T., Korenskiy, M., Pujol, O., Dubovik, O., Lopatin,
630 A.: Combined use of Mie-Raman and fluorescence lidar observations for improving aerosol
631 characterization: feasibility experiment, *Atm. Meas. Tech.*, 13, 6691–6701, 2020b.
632 doi.org/10.5194/amt-13-6691-2020.
- 633 Veselovskii, I., Hu, Q., Goloub, P., Podvin, T., Choël, M., Visez, N., and Korenskiy, M.: Mie–
634 Raman–fluorescence lidar observations of aerosols during pollen season in the north of France,
635 *Atm. Meas. Tech.*, 14, 4773–4786, 2021a. doi.org/10.5194/amt-14-4773-2021
- 636 Veselovskii, I., Hu, Q., Ansmann, A., Goloub, P., Podvin, T., Korenskiy, N.: Fluorescence lidar
637 observations of wildfire smoke inside cirrus: A contribution to smoke-cirrus - interaction
638 research, *Atmos. Chem. Phys. Disc.* 2021b. <https://doi.org/10.5194/acp-2021-1017>
- 639 Voudouri, K. A., Siomos, N., Michailidis, K., Papagiannopoulos, N., Mona, L., Cornacchia, C.,
640 Nicolae, D., and Balis, D.: Comparison of two automated aerosol typing methods and their
641 application to an EARLINET station, *Atmos. Chem. Phys.*, 19, 10961–10980, 2019.
642 <https://doi.org/10.5194/acp-19-10961-2019>
- 643 Wang, N., Shen, X., Xiao, D., Veselovskii, I., Zhao, C., Chen, F., Liu, C., Rong, Y., Ke, J., Wang,
644 B., Qi, B., Liu, D.: Development of ZJU high-spectral-resolution lidar for aerosol and cloud:
645 feature detection and classification, *Journal of Quantitative Spectroscopy & Radiative*
646 *Transfer*, v.261, 107513, 2021. doi.org/10.1016/j.jqsrt.2021.107513
- 647 Whiteman, D.N.: Examination of the traditional Raman lidar technique. II. Evaluating the ratios
648 for water vapor and aerosols, *Appl. Opt.*, 42, 2593–2608, 2003.
649 <https://doi.org/10.1364/AO.42.002593>

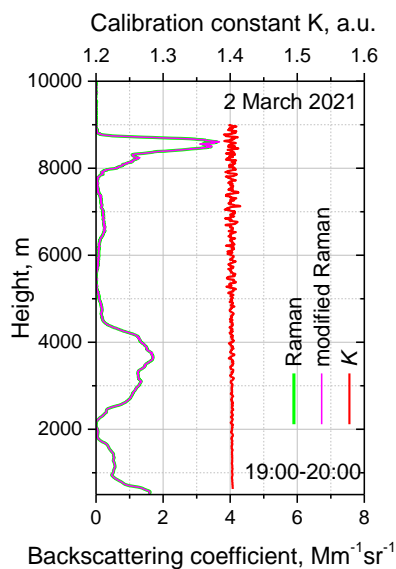


650 Zhang, Y., Li, Z., Chen, Y., Leeuw, G., Zhang, C., Xie, Y., and Li, K.: Improved inversion of
651 aerosol components in the atmospheric column from remote sensing data, *Atmos. Chem.*
652 *Phys.*, 20, 12795–12811, 2020. <https://doi.org/10.5194/acp-20-12795-2020>
653 Zhang, Y., Sun, Z., Chen, S., Chen, H., Guo, P., Chen, S., He, J., Wang, J., Nian, X.:
654 Classification and source analysis of low-altitude aerosols in Beijing using fluorescence–Mie
655 polarization lidar, *Optics Communications*, 479, 126417, 2021.
656 <https://doi.org/10.1016/j.optcom.2020.126417>
657
658



659

660



661

662 Fig.1. Backscattering coefficients at 532 nm for period 19:00 – 20:00 UTC on 2 March 2021

663 calculated from Mie-Raman observations using the reference height (green) and the calibration

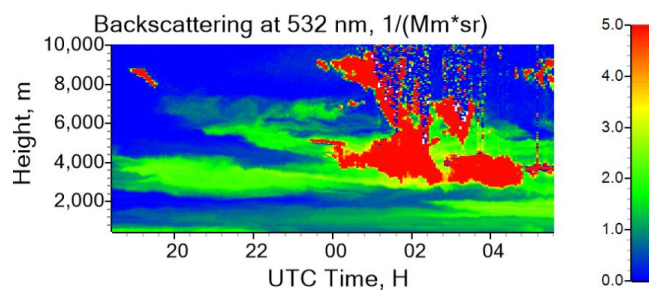
664 constant K (magenta). Calibration constant is shown with red line.

665

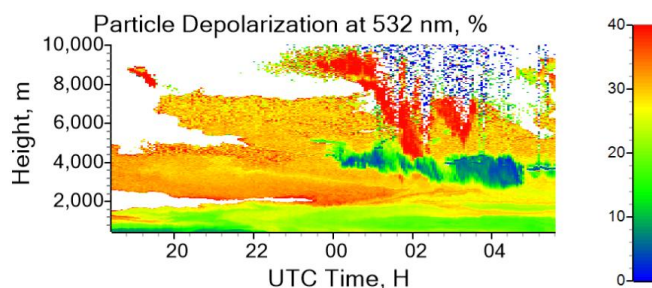
666



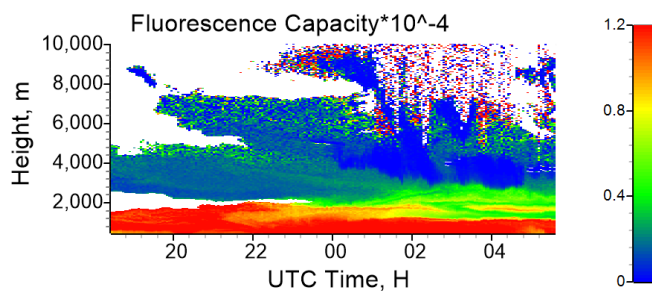
667
668



669



670

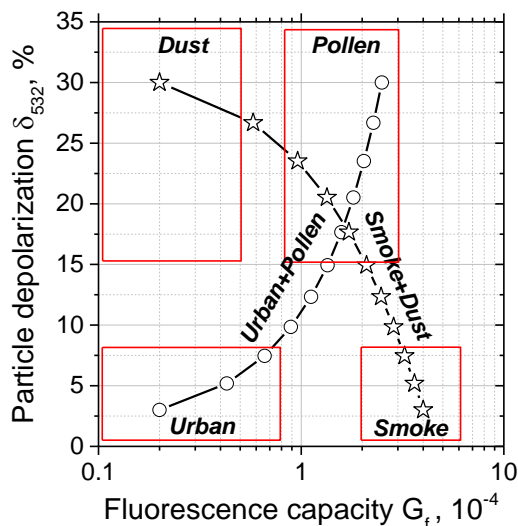


671

672 Fig.2. Spatio-temporal distributions of the backscattering coefficient β_{532} , the particle
673 depolarization ratio δ_{532} and the fluorescence capacity G_F in the night 2-3 March 2021. The
674 backscattering coefficient β_{532} is calculated with the modified Raman method. The values of δ_{532} ,
675 and G_F are shown for $\beta_{532} > 0.2 \text{ Mm}^{-1} \text{ sr}^{-1}$.
676



677



678
679
680
681
682
683
684

Fig.3. Aerosol typing with δ_{532} - G_F diagram. Chosen ranges of the particle parameters variation for dust, pollen, smoke and urban aerosol are shown by rectangles. The symbols show the results of simulation performed for pollen+urban (circles) and smoke + dust (stars) mixtures. Relative contribution of pollen (smoke) to the total backscattering β_{532} varied in 0 – 1.0 range with step 0.1. Particle parameters used in calculations are given in the text.



685

686

687

688

689

690

691

692

693

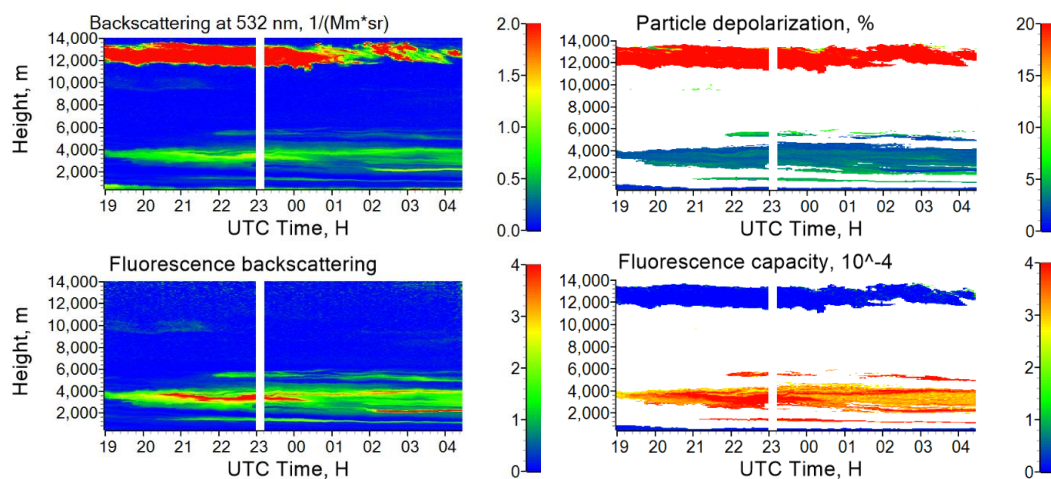


Fig.4. Spatio-temporal distributions of the backscattering coefficient β_{532} , the fluorescence backscattering coefficient β_F (in $10^{-4} \text{ Mm}^{-1} \text{ sr}^{-1}$), the particle depolarization ratio δ_{532} ; and the fluorescence capacity G_F in the night 12-13 September 2020. Calculation of δ_{532} and G_F was not performed for $\beta_{532} < 0.2 \text{ Mm}^{-1} \text{ sr}^{-1}$.

694

695

696

697

698

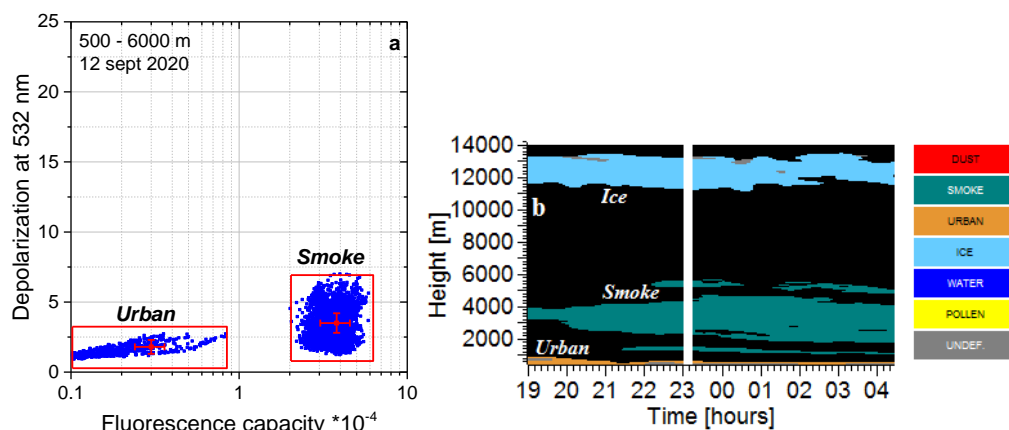


Fig.5 (a) The δ_{532} - G_F diagram for data from Fig.4 in 500 – 6000 m height range; (b) spatio-temporal distribution of aerosol types in the night 12-13 September 2020.



699
 700

701

702
 703
 704
 705
 706

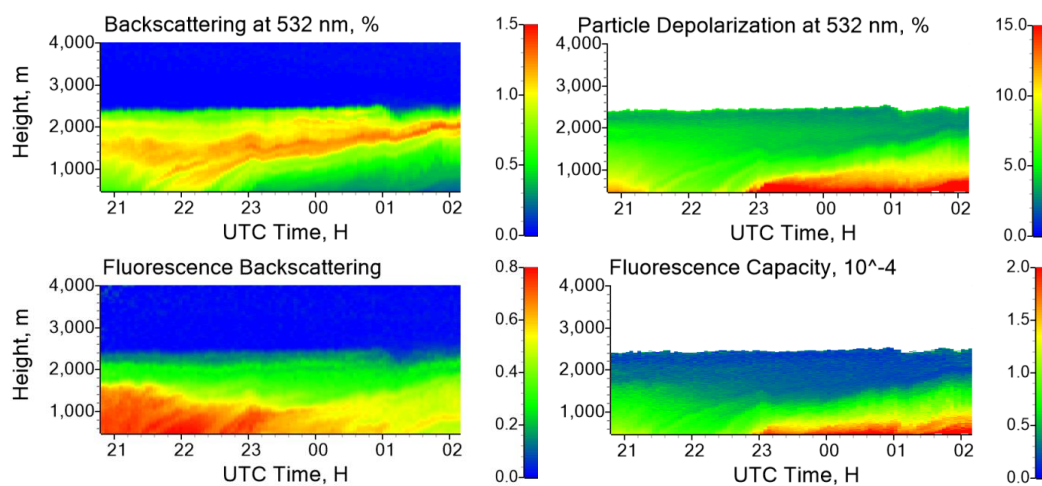
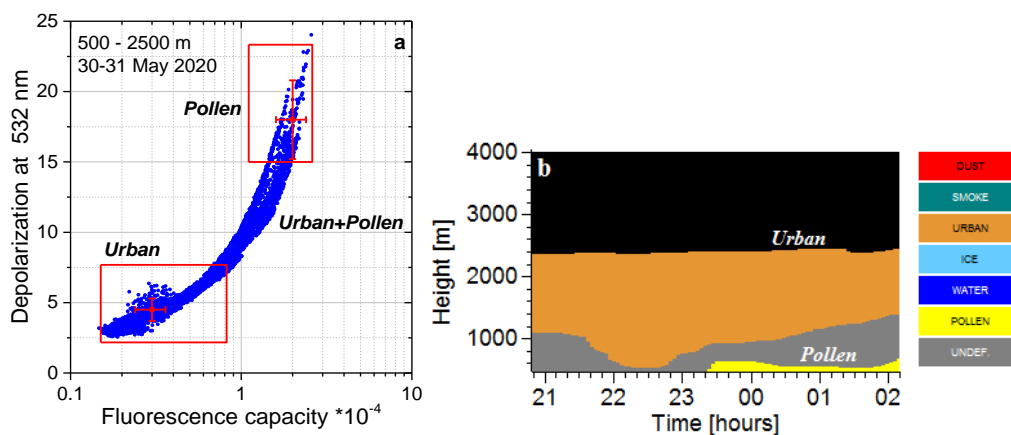


Fig.6. Spatio-temporal distributions of the backscattering coefficient β_{532} ; the fluorescence backscattering coefficient β_F (in $10^{-4} \text{ Mm}^{-1} \text{ sr}^{-1}$); the particle depolarization ratio δ_{532} ; and the fluorescence capacity G_F in the night 30-31 May 2020.

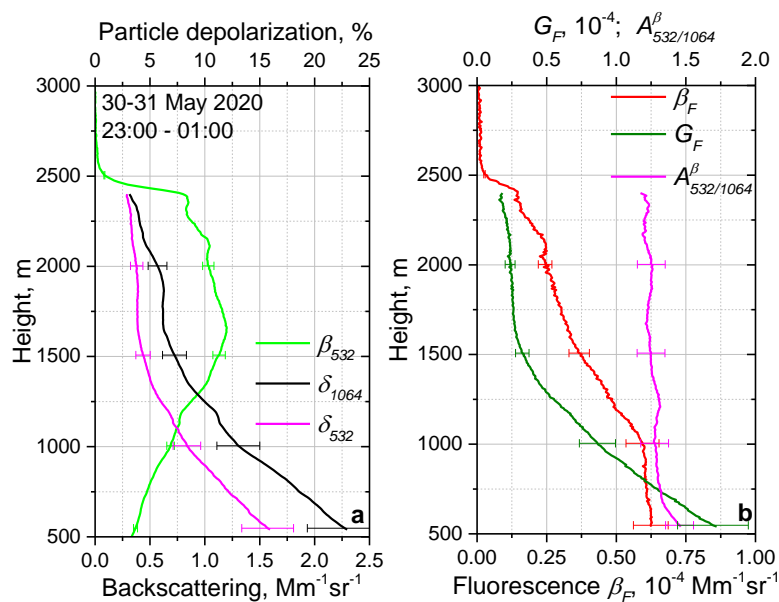


707
 708
 709
 710

Fig.7. (a) The δ_{532} - G_F diagram for observations in 500 m – 2500 m height range and (b) spatio-temporal distribution of aerosol types on the night 30-31 May 2020.



711



712

713 Fig.8. Vertical profiles of (a) backscattering coefficient β_{532} and particle depolarization ratios

714 δ_{532} , δ_{1064} ; (b) fluorescence backscattering β_F , fluorescence capacity G_F and backscattering

715 Angstrom exponent $A_{532/1064}^\beta$ on 30 May 2020 for period 21:00 – 23:00 UTC.

716



717

718

719

720

721

722

723

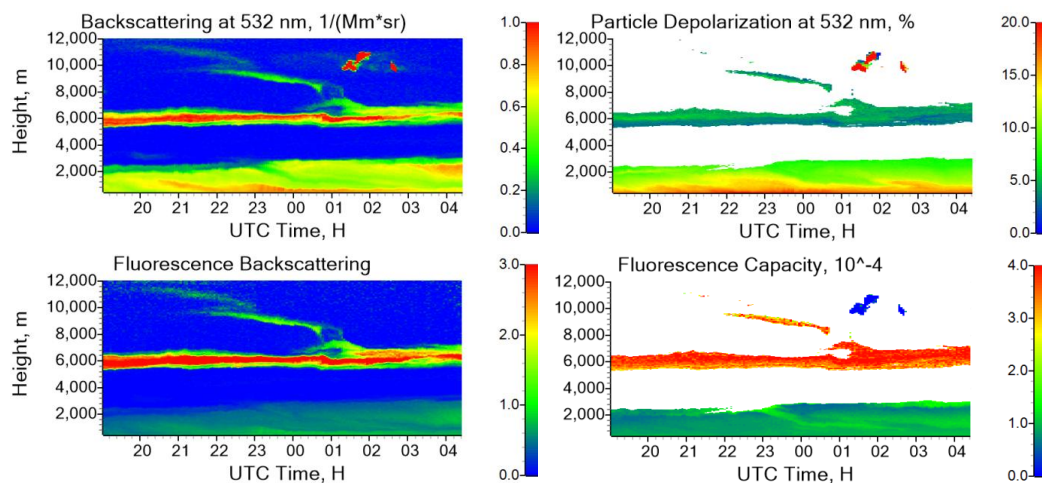


Fig.9. Spatio-temporal distributions of the backscattering coefficient β_{532} , the fluorescence backscattering coefficient β_F (in $10^{-4} \text{ Mm}^{-1} \text{ sr}^{-1}$), the particle depolarization ratio δ_{532} , and the fluorescence capacity G_F in the night 14 – 15 September 2020.

724

725

726

727

728

729

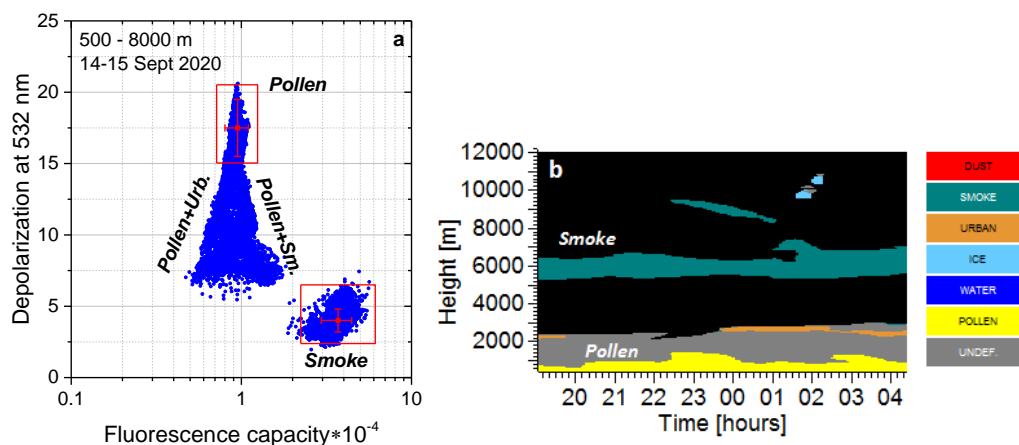
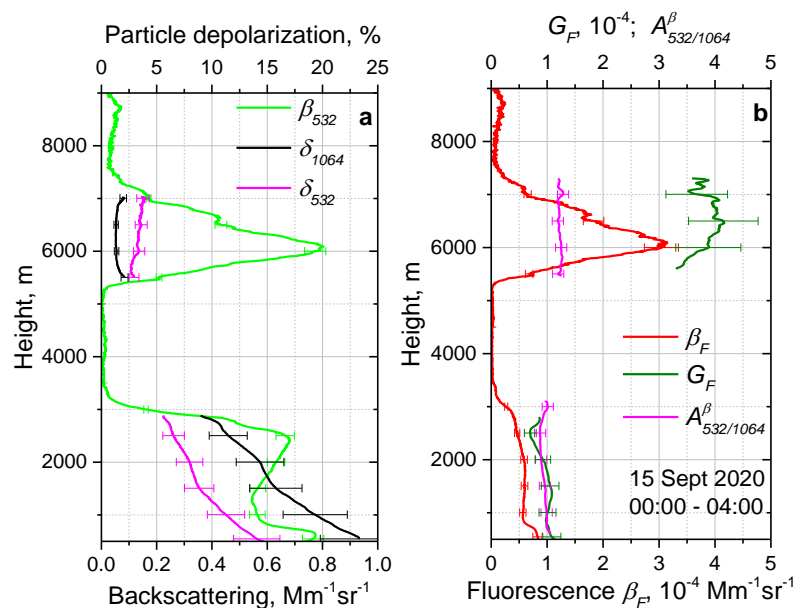


Fig.10. (a) The δ_{532} - G_F diagram for observations in 500 m – 8000 m height range and (b) spatio-temporal distribution of aerosol types in the night 14 – 15 September 2020.



730



731

732 Fig.11. Vertical profiles of (a) backscattering coefficient β_{532} and particle depolarization ratios

733 δ_{532} , δ_{1064} ; (b) fluorescence backscattering β_F , fluorescence capacity G_F and backscattering

734 Angstrom exponent $A_{532/1064}^\beta$ on 15 September 2020 for period 00:00 – 04:00 UTC.

735



736

737

738

739

740

741

742

743

744

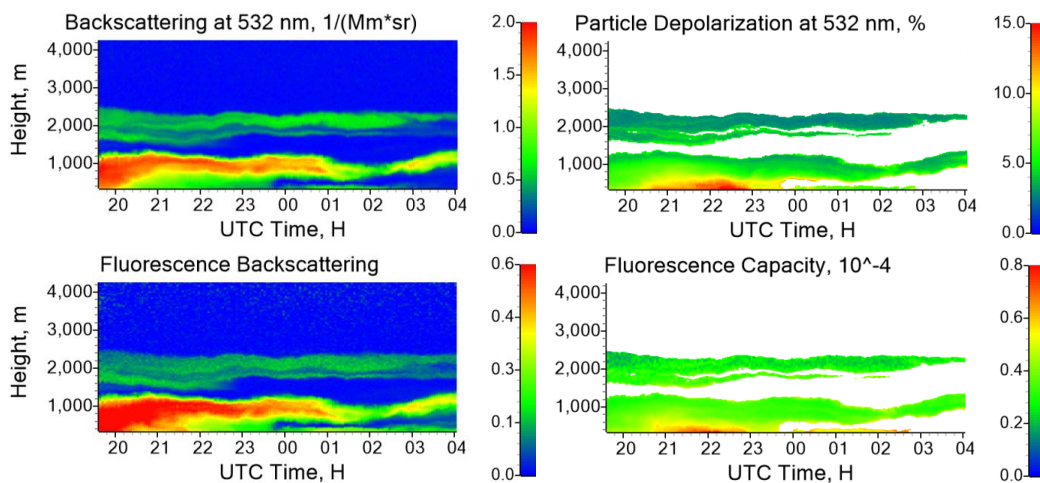
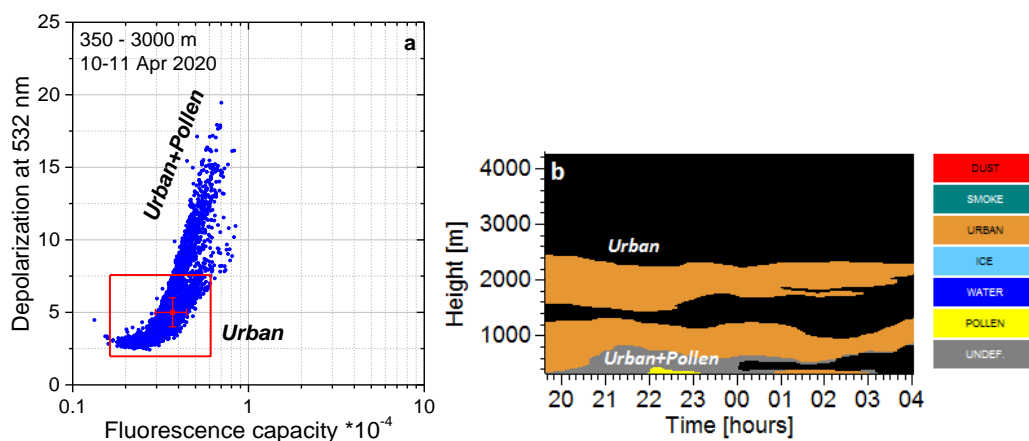


Fig.12. Spatio-temporal distributions of the backscattering coefficient β_{532} , the fluorescence backscattering coefficient β_F (in $10^{-4} Mm^{-1}sr^{-1}$), the particle depolarization ratio δ_{532} ; and the fluorescence capacity G_F in the night 10 – 11 April 2020. Measurements are performed at an angle of 45 dg to horizon.



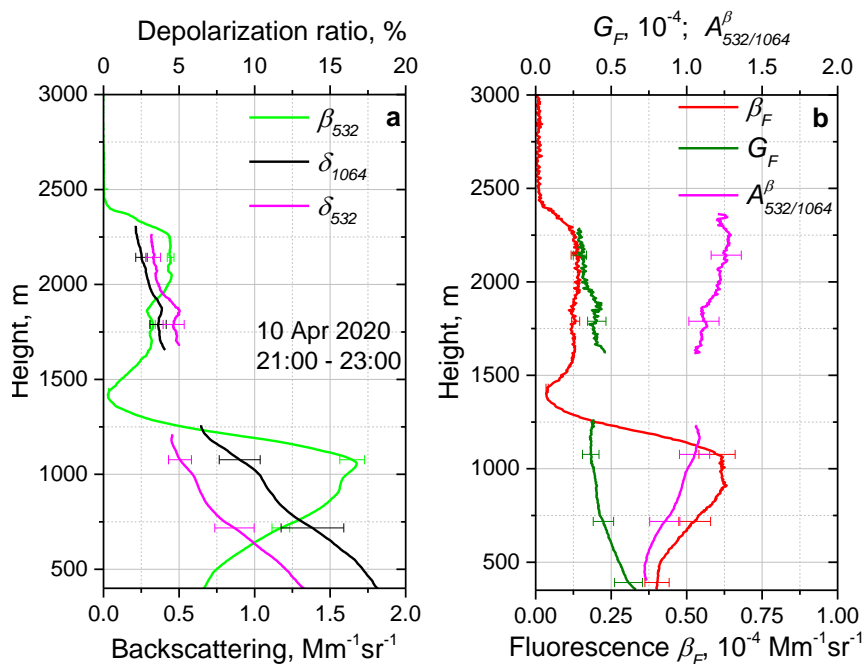
745

746

747

748

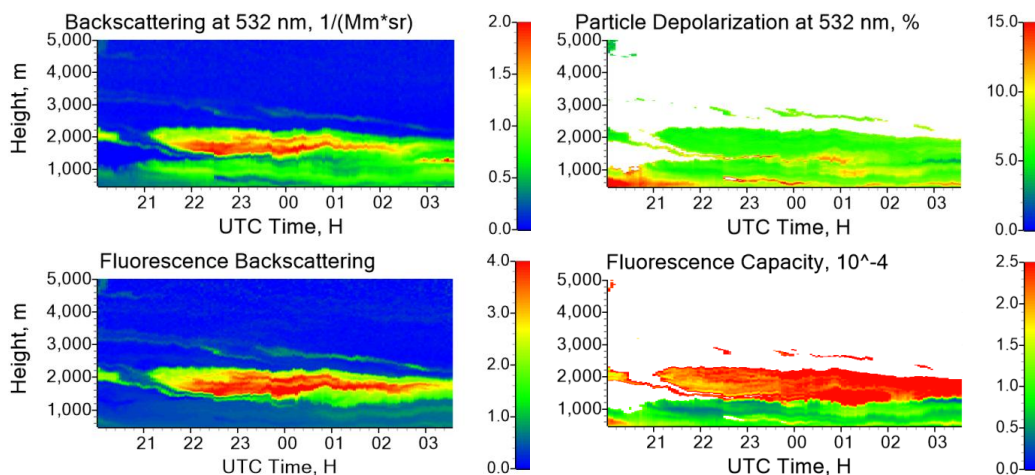
Fig.13. (a) The δ_{532} - G_F diagram for observations in 350 – 3000 m height range and (b) spatio-temporal distribution of aerosol types in the night 10 – 11 April 2020.



749
 750 Fig.14. Vertical profiles of (a) backscattering coefficient β_{532} and particle depolarization ratios
 751 δ_{532} , δ_{1064} ; (b) fluorescence backscattering β_F , fluorescence capacity G_F and backscattering
 752 Angstrom exponent $A_{532/1064}^\beta$ on 10 April 2020 for period 21:00 – 23:00 UTC.
 753



754



755

756

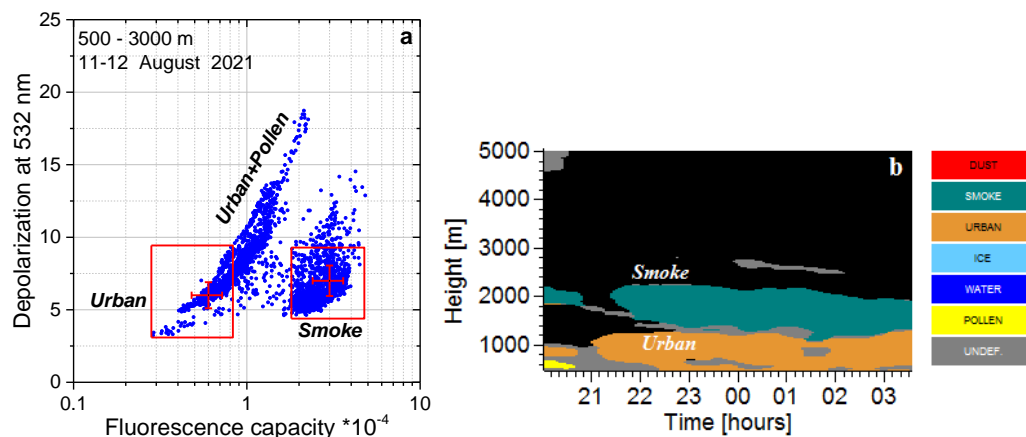
757

758

759

760

Fig.15. Spatio-temporal distributions of the backscattering coefficient β_{532} , the fluorescence backscattering coefficient β_F (in $10^{-4} \text{ Mm}^{-1}\text{sr}^{-1}$), the particle depolarization ratio δ_{532} , and the fluorescence capacity G_F in the night 11 – 12 August 2021.



761

762

763

764

765

766

Fig.16. (a) The δ_{532} - G_F diagram for observations in 500 – 3000 m height range and (b) spatio-temporal distribution of aerosol types in the night 11-12 August 2021.



767

768

769

770

771

772

773

774

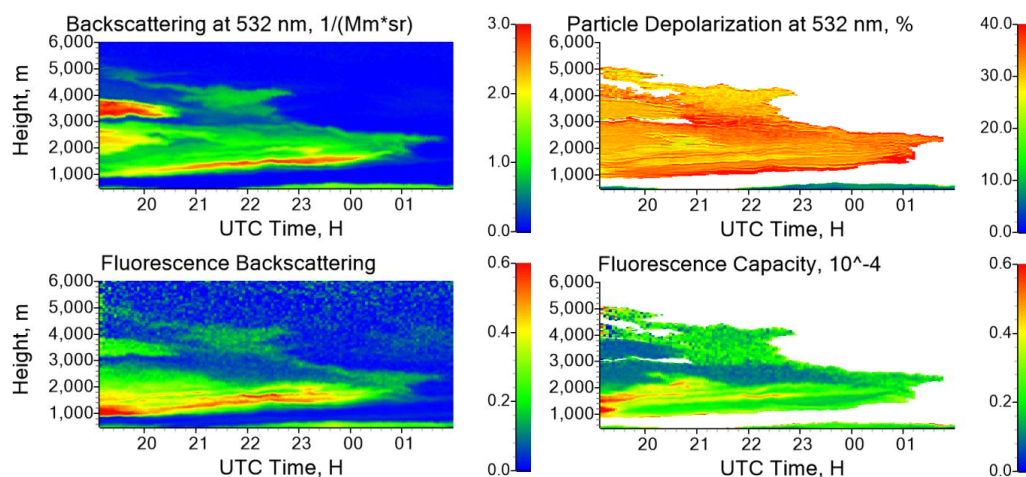
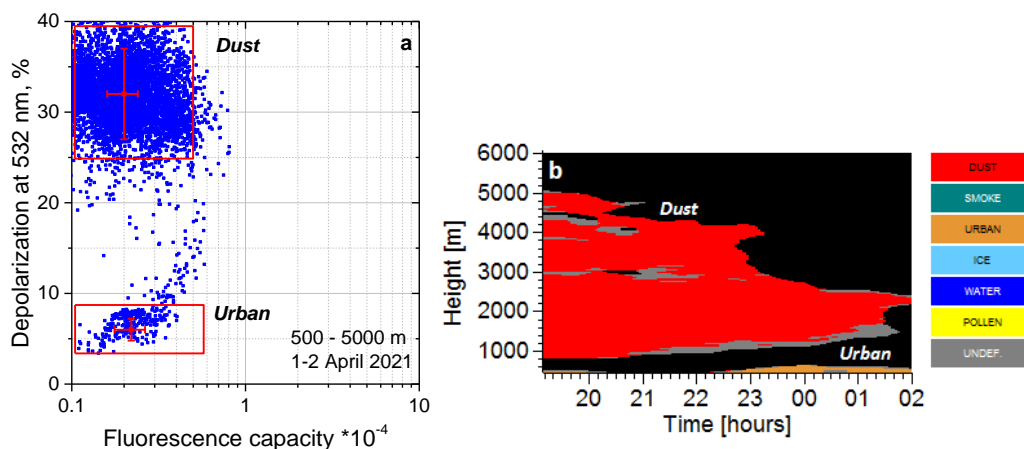


Fig.17. Height – temporal distributions of the backscattering coefficient at 532 nm β_{532} , the fluorescence backscattering coefficient β_F (in $10^{-4} \text{ Mm}^{-1}\text{sr}^{-1}$), the particle depolarization ratio at 532 nm δ_{532} , and the fluorescence capacity G_F in the night 1-2 April 2021. For the values $\beta_{532} < 0.2 \text{ Mm}^{-1}\text{sr}^{-1}$ the δ_{532} and G_F were not calculated.



775

776

777

778

779

780

781

782

Fig.18. (a) The δ_{532} - G_F diagram for observations in 500 – 5000 m height range and (b) spatio-temporal distribution of aerosol types in the night 1-2 April 2021.